



Forces and temperature variation during friction stir welding of aluminum alloy AA6082-T6

F. Lambiase¹ · A. Paoletti¹ · A. Di Ilio¹

Received: 23 March 2018 / Accepted: 30 July 2018
© Springer-Verlag London Ltd., part of Springer Nature 2018

Abstract

The variation of forces, torque, absorbed energy, and temperature distribution during friction stir welding process is investigated. Friction stir welding experiments were performed on an aluminum Al-Si-Mg alloy varying the tool rotation speed and the welding speed. An instrumented milling machine equipped with 3-axis load cell was adopted to measure the forces during the process. Temperature measurements were performed by means of an IR camera. A significant increase in temperature was observed during the process due to a “process preheating effect.” This resulted in the variation of the main forces. Phenomenological models were developed to describe these trends. The results indicated that processing conditions involving higher energy produced higher variation of temperature during the process, up to $2.3\text{ }^{\circ}\text{C mm}^{-1}$.

Keywords Friction stir welding · Forces · Energy · Temperature measurement · Specific energy · Power

1 Introduction

Lightweight structures are increasingly manufactured and employed with the aim of increasing performances, lowering the energy consumption and emissions. Thus, especially, high-strength aluminum alloys are strongly demanded by transportation industries, e.g., for body in white. When joining aluminum components, different welding processes can be adopted including electric arc, plasma, laser beam, or electron beam to produce continuous joints. These processes are affected by a number of limitations. The superficial oxide layer should be removed by pre-processes as well as preparation of the edges (e.g., chamfer). External material is often adopted (with the increase in weight and costs). In addition, welding processes generally involve great energy absorption, production of fumes and flashes along with high temperature, which leads to large heat-affected zones.

Friction stir welding (FSW) employs a non-consumable rotating tool that moves along the welding line. The tool provides both external heating (generated by friction between the tool and the workpiece) and plastic deformation of the materials (stirring effect). This highly localized heating softens the material around the pin and under the shoulder. Thus, the relative motion of the tool-workpieces along with the tool rotation induces the material to flow from the front of the tool to the back region, resulting in the stirring action. In addition, the tool shoulder exerts an upsetting action that enhances the materials' mixing. During FSW of metals, the material shows a pasty behavior and never yields the melting condition (solid-state joining process). Thus, the main defects generally involved with fusion welding, e.g., inclusions, porosities, cracks, and distortions, are avoided or highly limited.

Both thermal and mechanical aspects play a crucial role for the quality of the joints as well as for energy consumption. During FSW, the torque provides an indirect evaluation of the shear stress acting at the tool-workpiece interface, which in turn determines the heat generation and the plastic flow [1]. Thus, force and torque information is indicative of the weld quality. Nevertheless, only a few researches have been conducted to analyze the influence of the process parameters on the forces and temperature produced during FSW, as compared to those more focused on the microstructure and the strength of the joints. The influence of the process parameters on the force and torque was experimentally analyzed by Long

✉ F. Lambiase
francesco.lambiase@univaq.it

¹ Department of Industrial and Information Engineering and Economics, University of L'Aquila, Via Campo di Pile, 67100 L'Aquila, AQ, Italy

et al. [2] for different aluminum alloys. The authors determined the main relationships among the process input (the tool rotation speed) and process outputs (torque, longitudinal force, and grain size). Different equipment have been used to experimentally study the evolution of the forces during FSW. Das et al. [3] studied the influence of the processing parameters on the energy and main forces during hybrid joints made of AA6063 alloy and zinc-coated steel. Zimmer et al. [4] performed an experimental investigation concerning the influence of the FSW plunge processing parameters on the maximum generated force and torque. Su et al. [5] performed an indirect measurement of the main loads acting during FSW by measuring the power absorbed by the motors during the process. Jonckheere et al. [6] employed an expensive rotating dynamometer to monitor the tool torque during the process. Longhurst et al. [7] developed a torque control system to ensure constant energy to be supplied during the FSW process. Empirical, numerical, and also artificial neural network (ANN) models were also developed to understand the influence of the process parameters on the main forces during FSW. Cui et al. [8] developed a model for the prediction of the tool torque, the power, and the specific energy based on the process parameters. Manvatkar et al. [9] developed an artificial neural network to predict the peak temperature, the torque, and the welding force during FSW. The ANN was trained from the results of a nonlinear three-dimensional numerical model of FSW process. Similarly, Arora et al. [9] developed an ANN to predict the variation of the peak temperature, the torque, and the transverse force varying the main dimension of the tool.

The temperature field produced during FSW has been investigated by means of experimental analysis as well as numerical models. Yi et al. [10] studied the variation of the heat input during FSW of aluminum alloys by using calorimetric technique. Unfortunately, the experimental analysis based on the adoption of thermocouples involves many complications including breaking, precise positioning, and slipping out [6]. On the contrary, infrared thermography involving IR cameras represents an easier and more comprehensive tool. Beyond experimental approaches, several models have been developed to predict the thermal field during FSW [1, 11–13]. Khandkar et al. [14] developed an input torque-based model to predict the temperature distribution. El-Sayed et al. [15] developed a thermal FE model of FSW process to study the thermal stress produced by the heat supplied during the process. Meyghani et al. [16] developed a coupled thermo-mechanical simulation of the process to investigate the temperature distribution produced during the process. Su et al. [17] investigated the tool-workpiece interaction numerically, and particularly the influence of friction condition on the heat generated. Kumar et al. [18] analyzed the maximum temperature reached during FSW both experimentally and numerically and related the defects to the supplied heat input.

However, the abovementioned researchers focused on specific aspects: some of them focused on the forces and some others on the temperature field. In addition, many of them referred to average values of the signals (temperature, forces, and torque), while these signals can vary significantly during the process. The present investigation tries to overcome the abovementioned limitations. Actually, a comprehensive analysis of the forces (welding and plunging), the torque, and the temperature was conducted by using an instrumented milling machine. To this end, load and position sensors as well as an IR camera were involved. Thus, both the mean values and the trends of these signals were analyzed during the process to verify how much the process conditions vary during FSW.

2 Materials and methods

2.1 Specimen preparation

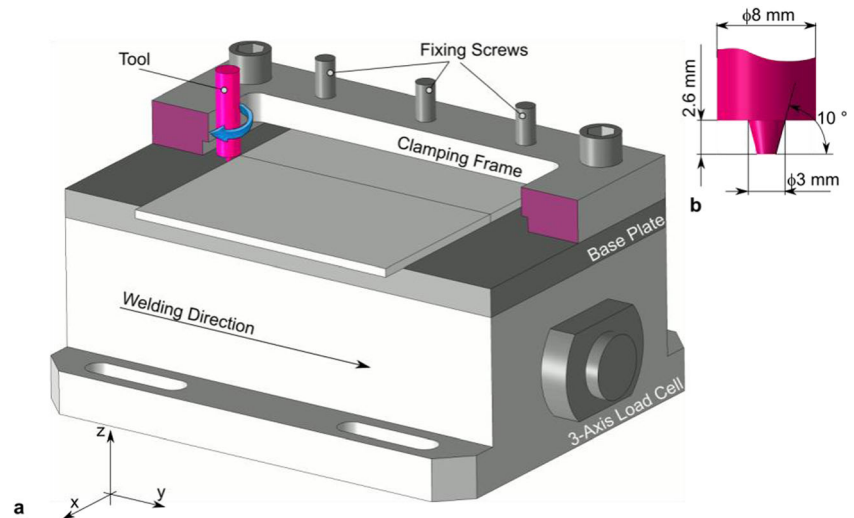
Rolled sheets with 3.0 mm of thickness of AA6082-T6 aluminum alloy were joined in butt configuration. The specimens were cut from a unique sheet by means of a bandsaw to a dimension of 60 mm × 100 mm (width × length). Then, the edges were grinded to ensure accurate correspondence of the faces. Before joining, the sheets were immersed in an ultrasonic bath (water and ethanol) to remove grease, oil, and powder. Then, they were covered by means of a thin graphite layer to increase the surface emissivity (to perform the IR temperature measurements during FSW process). This enabled to increase the surface emissivity up to 0.80. This value was determined by performing calibration tests according to the procedure reported in [19].

2.2 Joining procedure and measurements

Friction stir welding experiments were conducted by means of a 3-axis milling machine. A schematic representation of the equipment is depicted in Fig. 1. The sheets are fully in contact with the underlying steel plate, while they are clamped by means of six “fixing screws” with an end tip. This enabled to reduce the heat diffusion from the aluminum sheets to the overlying clamping frame. It also enabled to fully constraint the sheets during the joining process.

The bottom plate was mounted on a 3-axis piezoelectric transducer type 9257B by Kistler, which was connected to a charge amplifier type 5017 by Kistler. The force signals were then acquired by means of an I/O acquisition board model USB6009 by National Instrument at a sample rate of 6 kHz and then filtered and resampled by using a moving average filter (set at 1000 samples). After the acquisition, the raw data was converted into the three force components: F_x (force in transverse direction), F_y (force in welding direction) and F_z

Fig. 1 Schematic representation of (a) the experimental setup and principal directions and (b) main dimensions of the tool



(clamping force), and $M_{z(\text{tool})}$ (torque). The torque acting on the tool $M_{z(\text{tool})}$ was calculated by Eq. (1):

$$M_{z \text{ tool}} = M_{z \text{ cell}} - F_x \cdot y \quad (1)$$

The y position was measured by a linear variable differential transformer (LVDT) mounted on the milling machine at the same frequency of the force components. The actual power P was calculated as the product of the torque M_z (tool) by the tool rotation speed ω [rad/s]. The energy input (Q) was calculated by means of Eq. (2). Here, the tool rotation speed ω [rad/s] is constant throughout the process, and the torque M_z is measured instantly by the piezoelectric transducer.

$$Q = \int M_z \cdot \omega dt = \omega \int M_z dt \quad (2)$$

Temperature measurements were conducted by means of an infrared camera model E60 by FLIR. This enabled to measure the temperature evolution and its spatial distribution during the FSW process. An acquisition rate of 30 Hz was adopted. The camera was placed at an angle of 60° with respect to the aluminum sheet at almost 300 mm. The camera was fixed to the machine head with the aim of observing the temperature variation within a window fixed to the tool.

A cylindrical tool with a truncated cone end tip made of hardened K340 high-strength steel was used. A schematic representation of the experimental setup and the tool geometry is reported in Fig. 1a along with the main dimensions of the tool (Fig. 1b).

Friction stir welding experiments were conducted under position control using a constant welding speed. During the tests, the tool entered from a side edge. This avoided the presence of the plunging phase, which introduces a transitory during the process [4]. Six joining conditions were analyzed by

varying the welding speed and the tool rotation speed. A 2×3 experimental plan consisted in the combinations of all the levels for each factor. The adopted levels are summarized in Table 1. Three repetitions were performed for each joining condition. The plunging depth was kept constant at 0.1 mm in all experiments. The maximum and minimum values of the tool rotation speed and the welding speed were chosen based on preliminary tests and by considering the machine capability.

3 Results

3.1 Temperature measurement

Figure 2 depicts the typical IR image acquired during the FSW process. The IR thermographies enable to qualitatively observe the temperature distribution on the aluminum sheet surface along with quantitative measurements performed on different types of regions of interest (ROIs). Particularly, to determine the temperature variation of the material approaching the FSW tool, a rectangular ROI reported in Fig. 2 and named AR01 was drawn. Then, the maximum temperature over the area AR01 was determined for each frame. It must be concerned that, as the IR camera was mounted integral with the

Table 1 Experimental plan of FSW tests

Level	Tool rotation speed, ω (RPM)	Welding speed, v_f (mm/min)
I	800	14.5
II	1250	21
III		31

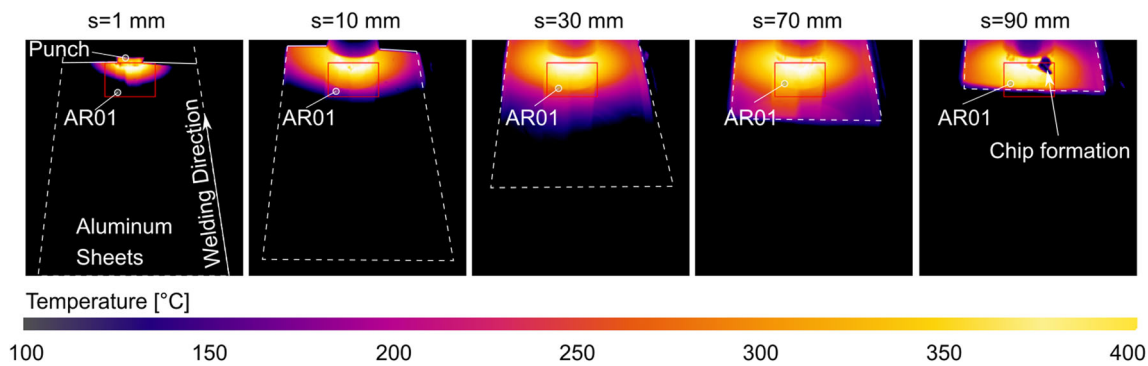


Fig. 2 IR image during FSW showing the area AR01 ($\omega = 800$ RPM and $v_f = 21$ mm/min). The welding direction indicates the movement of the aluminum sheets

machine head, the area AR01 always focused on a window with the same distance from the tool.

The adoption of the LVDT for the measurement of the tool-workpiece relative position enabled to analyze the variation of the temperature vs. the position(s) instead of the processing time. This enabled a better comparison of the temperature trends achieved with different welding speeds. The IR thermographies at different positions, e.g., $s = 1$ mm, $s = 10$ mm, and $s = 30$ mm, as shown in Fig. 2a–c, respectively, indicate that the temperature of the sheet increased during the process. This is qualitatively confirmed by the enlarged portion of the aluminum sheets that exceeds the threshold (minimum) temperature of the IR scale (black areas are below 100 °C). However, quantitative measurements were also performed to determine the temperatures resulting from the adoption of different process conditions.

Figure 3 depicts the variation of the maximum temperature measured over the area AR01 during FSW process. These temperature trends are characterized by different features. Initially, the temperature steeply increases as the tool enters in contact with the aluminum sheets. The processing conditions show a negligible influence on the value of the initial temperature with the exceptions of local peaks

and ranges between 240 and 260 °C. However, as the tool proceeds, the temperature rises almost linearly with a gradient depending on the processing conditions. Actually, the temperature of the material that is close to be stirred by the FSW tool (which is identified with the area AR01) increases due to a sort of “process preheating effect.” Then, as the tool is close to the exit region, the temperature undergoes a steeper increase as it is clearly depicted in Fig. 3a. The “preheating effect” was intrinsically observed in some simulations performed in previous studies [11, 13, 16, 20]. Actually, numerical simulations indicated that the temperature of the material in front of the tool was higher than the initial temperature. However, the influence of the process parameters on the magnitude of the “process preheating effect” was not yet investigated.

A schematic representation of the heat exchanges involved in the process is reported in Fig. 4, to better understand the aforementioned trends. It must be remembered that the area AR01 precedes the tool in the welding direction. Thus, during the FSW process, there are different heat fluxes acting on the AR01 region including a positive heat flux from the material in contact with the tool (Q_{IN}), a negative heat flux due to the heat loss towards the material ahead the AR01 region in the

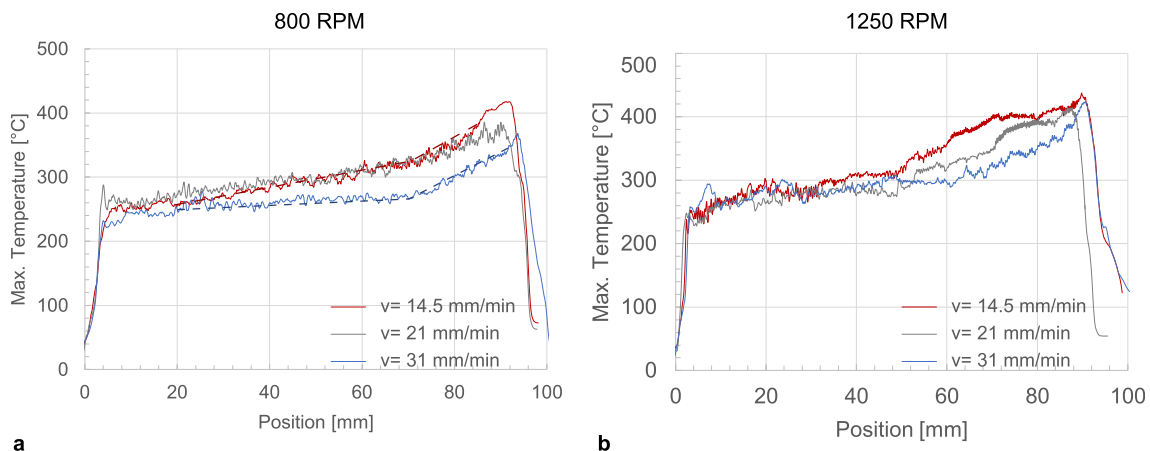
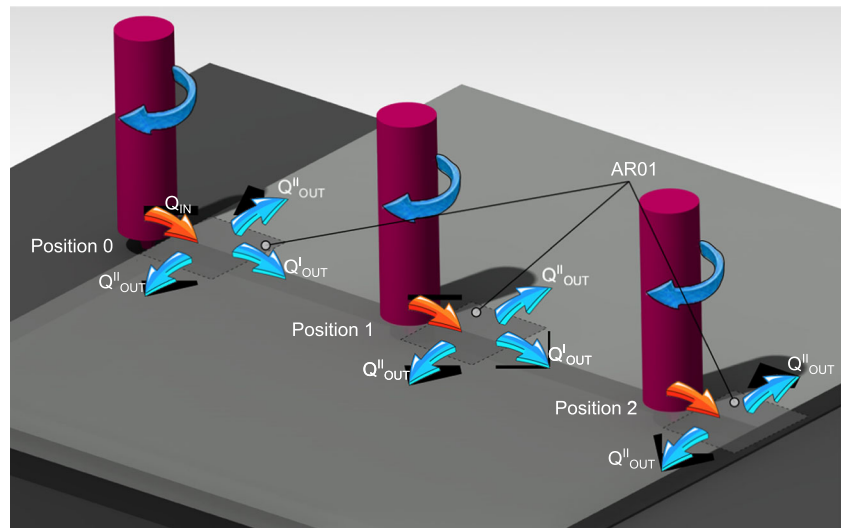


Fig. 3 Temperature trends determined over the area AR01 varying the processing conditions. Temperature trend: $\omega = 800$ RPM (a), $\omega = 1250$ RPM (b)

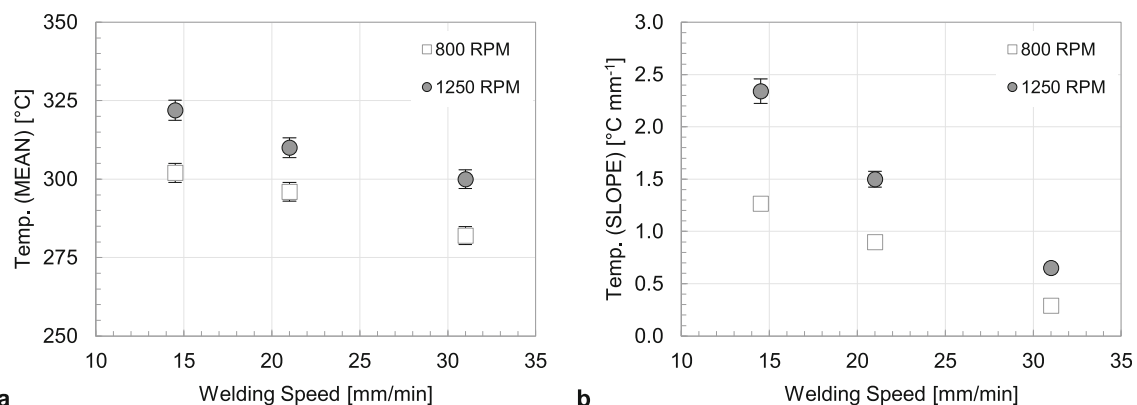
Fig. 4 Schematic representation of heat fluxes during FSW

welding direction (Q^I_{OUT}), and a negative heat flux due to the heat loss towards the material that surrounds the AR01 region in the side direction (Q^{II}_{OUT}). In addition, there are other fluxes due to convection and radiation towards the environment as well as the conductive heat flux towards the underlying plate and the clamping frame (which has been minimized as the limited contact surface). As Q_{IN} , Q^I_{OUT} , and Q^{II}_{OUT} are all of conductive nature, materials with higher thermal conductivity involve higher values of Q_{IN} , Q^I_{OUT} , and Q^{II}_{OUT} . The magnitude of these fluxes also depends on the temperature gradients between the region AR01 and the surrounding material. Furthermore, Q_{IN} directly depends on the process conditions, and particularly it increases with the tool rotation speed ω . In addition, Q_{IN} decreases with the welding speed v_b as it involves shorter interaction time. On the other hand, the amount of heat loss by conduction towards the surrounding material Q^I_{OUT} and Q^{II}_{OUT} reduces with the welding speed as shorter heat transfer time is involved.

At the beginning of the process, the temperature within the AR01 region is $T_0 \approx 30^\circ\text{C}$. However, as soon as the tool

enters in contact with the sheets (position 0), the temperature of the region AR01 suddenly increases (as shown in Fig. 3) and, as the tool proceeds (position 1), it enters in contact with a preheated material leading to the aforementioned increase in temperature (both maximum and average). Finally, as the tool approaches the exit region, the heat loss by conduction Q^I_{OUT} reduces (as there is lower material ahead the AR01 region) leading to higher heat stored within the area AR01 with consequent steeper increase in temperature, as shown in Fig. 3).

Figure 5 depicts the variation of the average temperature measured over the position window 20–70 mm (as shown in Fig. 3) as well as the trends of the gradient in the same window. It is clear that the mean temperature (over the area AR01) increases with the tool rotation speed as higher friction heat is produced at the interface leading to higher temperature. The temperature in the region AR01 decreases almost linearly with the welding speed as lower interaction time is involved (lower preheating effect). These trends are consistent with the results reported in [15, 21]. Similarly,

**Fig. 5** Influence of the process conditions on the maximum temperature within the region AR01 and temperature gradient

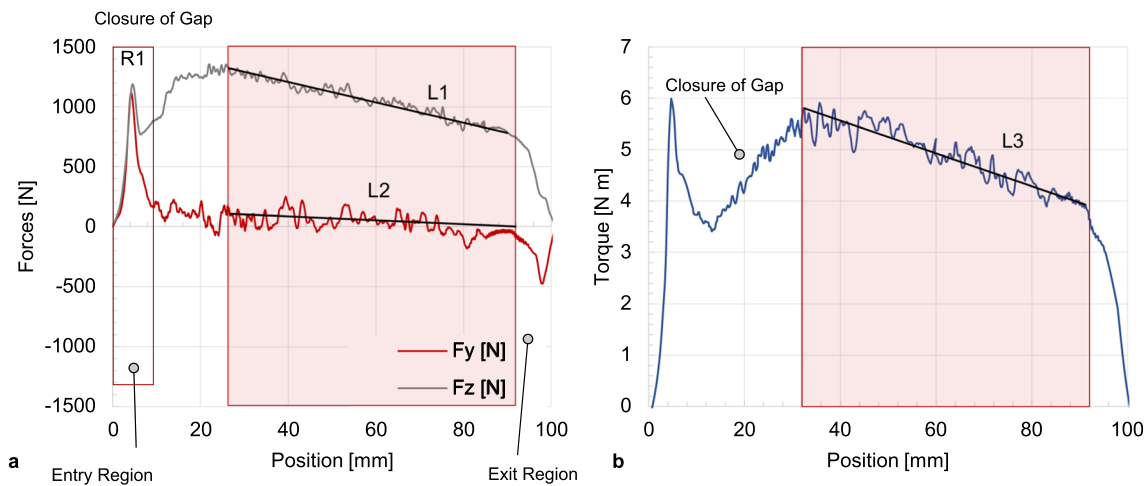


Fig. 6 Variation of the welding (F_y) and plunging (F_z) forces (a) and torque (b) acting on the tool

temperature gradients decrease with the welding speed and increase with the tool rotation speed, as shown in Fig. 5b. Actually, higher tool rotation speed ($\omega = 1250$ RPM) involves higher values of the Q_{IN} heat flux. Thus, higher heat is stored in the material that is close to be stirred with respect to the cases involving lower rotation speed ($\omega = 800$ RPM). On the other hand, the increase in the welding speed involves lower temperature gradients as lower energy is supplied for preheating. Beyond the aforementioned trends, the absolute values of the temperature gradients are worth noting; actually, for $\omega = 800$ RPM, these gradients are in the range $0.3\text{--}1.27\text{ }^{\circ}\text{C mm}^{-1}$ while for $\omega = 1250$ RPM, they rise to $0.65\text{--}2.34\text{ }^{\circ}\text{C mm}^{-1}$. These results indicate that the temperature of the weld can increase more than $200\text{ }^{\circ}\text{C}$ along a weld of 100 mm.

3.2 Force analysis

The variation of the main forces acting on the tool during friction stir welding process is reported in Fig. 6a, b. The force variation is mainly due to temperature changes that influence the flow stress. However, at the entry and exit regions, the variation of the forces is also due to that of the contact surfaces. At the entry region, both the welding force (F_y) and the plunging force (F_z) show a sudden increase followed by a steep drop, as shown by the rectangle R1 depicted in Fig. 6a. The increase of F_y and F_z is due to the enlargement of the contact surface, as schematically depicted in Fig. 7. After reaching the first peak, F_y and F_z show different trends: the welding force reduces significantly and reaches an almost steady state, while the plunging force gets back to increase.

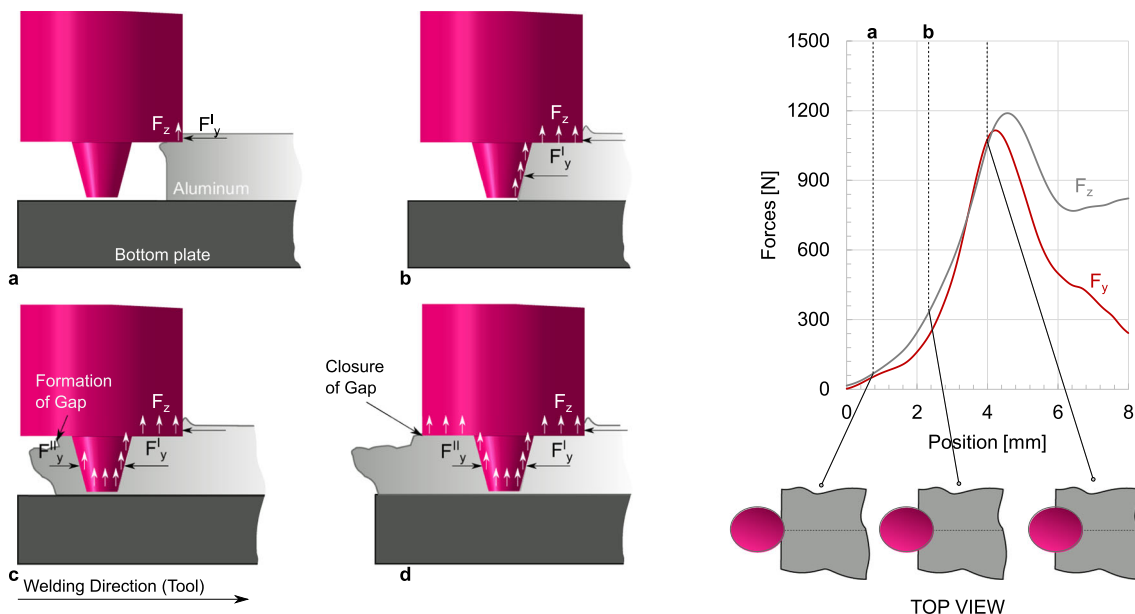


Fig. 7 Effect of contact surface evolution on plunging and welding forces

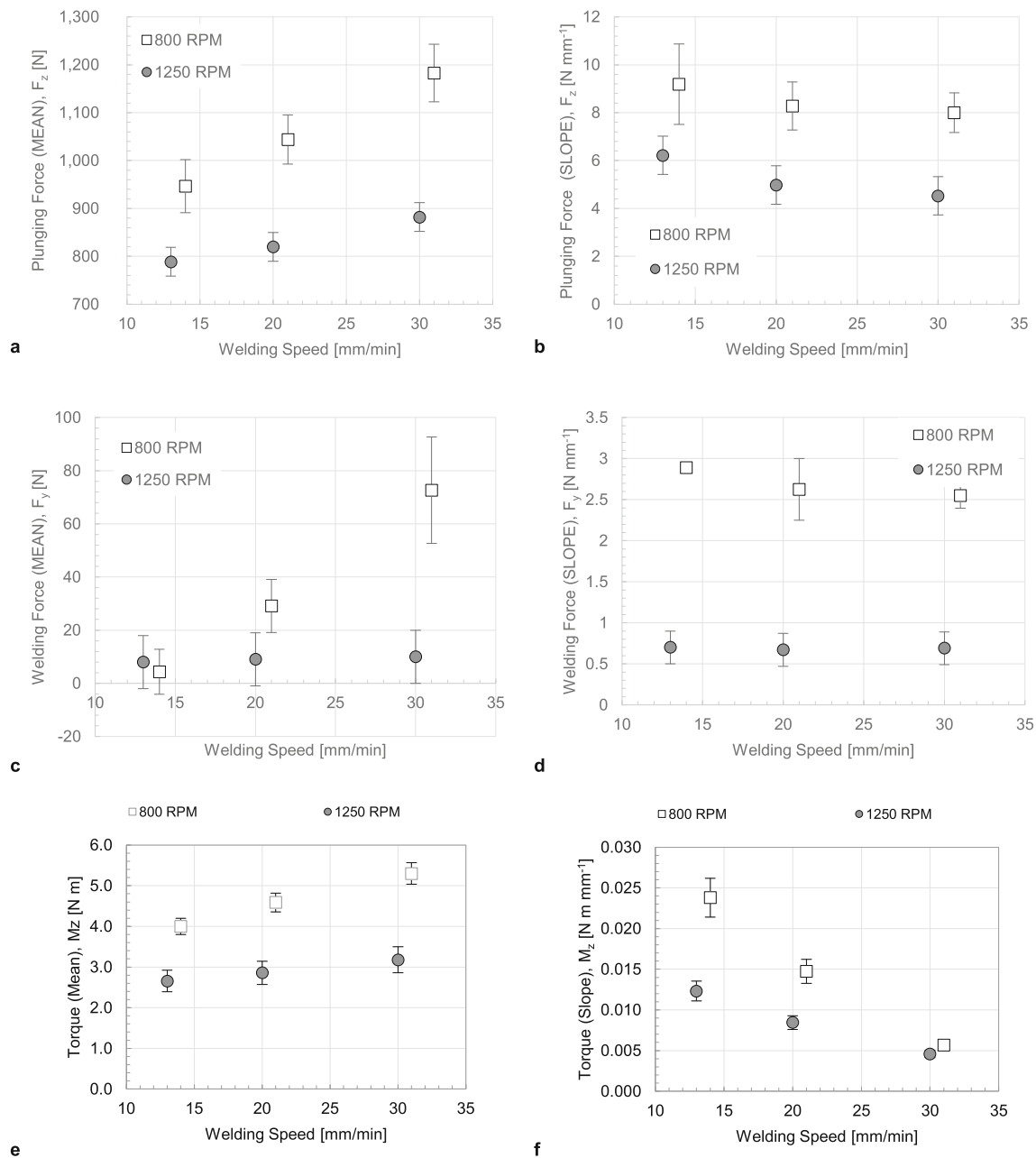


Fig. 8 Effect of process parameters on mean values and gradients of plunging force, welding force, and torque

Again, these different trends can be explained by considering the tool-sheets contact surfaces. At the beginning, the tool enters in contact with the sheets (Fig. 7a). Thus, the component F_y^I , which opposes to the tool motion, develops on the tool pin and the tool shoulder plunged in the sheets (Fig. 7b). After the tool pin has completely entered (almost 5 mm), a negative component F_y^{II} develops in the opposite direction and partially compensates the component F_y^I (Fig. 7c). This leads to a reduction of the overall welding force F_y . The presence of the negative component F_y^{II} is also confirmed by the negative values of the force at the exit region. Here, the missing material in front of the tool leads to a

drastic reduction of the component F_y^I . On the other hand, after the first peak, the F_z and M_z trends show a different behavior as compared to F_y . Indeed, after reaching a minimum value due to the material softening, both F_z and M_z get back to increase due to the increase in the contact surface. However, this increase does not develop as soon as the tool has completely entered (8 mm) but rather it develops more gradually as the formation of a gap between the sheets and its subsequent closure (Fig. 7d).

Despite the abovementioned features that mainly develops when in entry and exit regions (avoiding the common plunging and the tool retraction phases), it is worth noting that in the

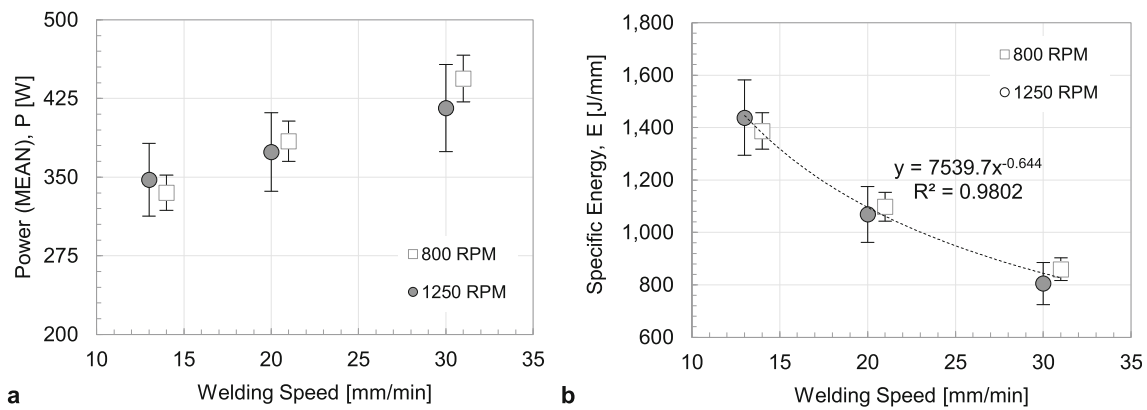


Fig. 9 Influence of process parameters on mean power P and specific energy E

central region, the forces F_y and F_z and the torque M_z do not keep constant but rather they show monotonic trends. Thus, to better understand these trends, they were analyzed within the window highlighted in Fig. 6 and the linear fits of these trends (L1 for F_z , L2 for F_y , and L3 for M_z) were characterized by considering the mean values and the gradients.

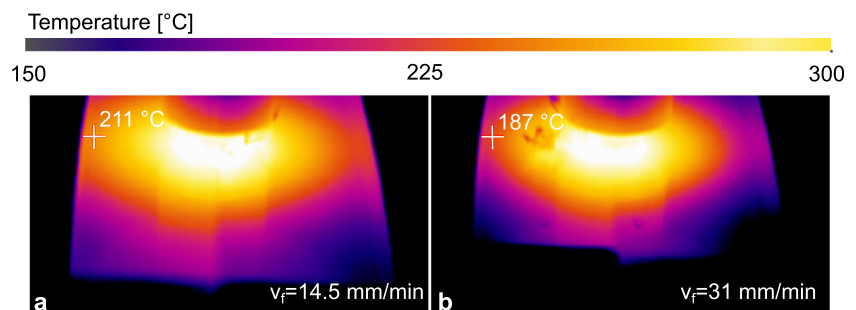
All the mean values of the plunging force F_z , the welding force F_y , and the torque M_z increase with the welding speed while decrease with the tool rotation speed. These trends are consistent with those reported in a number of literature works [3–5] and are due to the reduction of the flow stress. The plunging force F_z is almost an order of magnitude higher than the welding force F_y . This is due to the aforementioned opposite components F_y^I and F_y^{II} of the welding force that oppose each other and result into a drastic reduction of the resulting F_y force acting on the tool. However, it can be also addressed to the low plunging depth of the tool that significantly reduces the welding force. Since the aforementioned variation of the temperature during the process, also the main forces show a reduction during the FSW process due to the material softening. The magnitude of these variations, which is measured by the gradients of the fitting curves L1, L2, and L3, has been reported in Fig. 8b, d, and e. As it can be inferred, the force gradient decreases with the welding speed and the tool rotation speed. Actually, higher welding speeds involve lower temperature variations in the material to be stirred (region AR01). This yields to lower variations of

the welding force, plunging force, and the torque. On the other hand, the influence of the tool rotation speed on the gradients of the forces and torque is less marked. Indeed, based on the influence of the tool rotation speed on the temperature gradient, it could be expected that the increase in the tool rotation would determine higher gradients in the forces and torque, while the opposite trend was observed. A possible reason may lie in the effective temperature of the material in contact with the tool. Please note that the temperatures reported in Fig. 5a refer to the material in front of the tool and not under the tool pin. When the tool rotation speed $v_f = 1250$ RPM was adopted, the material under the tool was much more pasty as compared to the case $v_f = 800$ RPM. This is also evident by the great difference between the welding force of test performed at 800 RPM and 1250 RPM reported in Fig. 8c. Thus, for $v_f = 1250$ RPM, high variation in the temperature produced small changes in the material yield stress.

The influence of the process parameters on the power P was calculated as the product of the torque M_z by the tool rotation speed ω : $P = M_z \times \omega$. Similarly, the specific energy E , which represents the energy required to produce a weld of 1 mm, was calculated as: $E = P \times 60/v_f$.

The results reported in Fig. 9a indicate that the power increased almost linearly with the welding speed because of the increase of M_z with v_f . On the other hand, P is affected slightly by the tool rotation speed. On the other hand, the specific

Fig. 10 Influence of the welding speed v_f on the temperature reached at peripheral regions



energy E decreased with the welding speed and follows a negative exponential law. This result is consistent with the experimental findings reported in [22]. Actually, low welding speeds involve longer interaction times even though they are characterized by lower power requirements. This leads to higher specific energy requirement. Actually, under low welding speeds, higher energy is lost due to heat exchange towards the tool, the underlying support, as well as the surrounding material as it is clearly visible from the IR thermographies reported in Fig. 10. Here, the same points (positioned at 17 mm from the tool axis) showed a significant difference of temperature that indicates a higher heat loss by conduction when lower welding speeds are involved.

4 Conclusions

The comprehensive monitoring of the forces and temperature during FSW represents a useful approach to understand the mutual influence between temperature and forces. This also enables to deeply study the effect of the process parameters on process parameters such as the power and the specific energy. Under the analyzed processing window, FSW of aluminum alloy involved significant variations of the temperature and main forces. The results quantified the influence of the processing conditions on the temperature and force variations during FSW.

Conditions being characterized by higher tool rotation speed and low welding speed involved significant increase in temperature along the welding line. This was due to a “process preheating effect.” The variation in temperature was in the range 0.3–2.3 °C/mm; the mean values of the forces increased with the welding speed and reduced with the tool rotation speed as these conditions involved lower temperatures of the material being stirred and consequently higher flow stress.

A descriptive model of the force distribution was proposed to understand the variation of the forces during FSW. The model was introduced to explain the different behaviors of the plunging force and the welding force even during entry and exit regions; the aforementioned variation in temperature influenced the welding force, the plunging force, and the torque because of the different material conditions being stirred and consequently different flow stress.

The results indicated that the welding speed influenced significantly the power involved and the specific energy. On the contrary, negligible effect of the tool rotation speed was observed. The power increased with the welding speed, while the specific energy reduced with the welding speed. This behavior was addressed to the increase of heat loss by conduction towards the surrounding material.

The main drawbacks of the study are represented by the limited range of welding speeds that were analyzed. This was

due to the limited capabilities of the milling machine involved. This will drive future studies to develop and adopt more performing equipment to increase the welding speed and consequently enable this kind of analysis for higher welding speeds. As the variation of the temperature is the main cause of the force variation, also the analysis of the tool geometry and material of the clamping system on the temperature and forces may represent a key aspect influencing the FSW process and quality of joints.

Publisher's Note Springer Nature remains neutral with regard to jurisdictional claims in published maps and institutional affiliations.

References

1. Bhattacharya TK, Das H, Jana SS, Pal TK (2016) Numerical and experimental investigation of thermal history, material flow and mechanical properties of friction stir welded aluminium alloy to DHP copper dissimilar joint. *Int J Adv Manuf Technol* 88(1–4): 847–861
2. Long T, Tang W, Reynolds AP (2013) Process response parameter relationships in aluminium alloy friction stir welds. *Sci Technol Weld Join* 12(4):311–317
3. Das H, Basak S, Das G, Pal TK (2012) Influence of energy induced from processing parameters on the mechanical properties of friction stir welded lap joint of aluminum to coated steel sheet. *Int J Adv Manuf Technol* 64(9–12):1653–1661
4. Zimmer S, Langlois L, Laye J, Bigot R (2009) Experimental investigation of the influence of the FSW plunge processing parameters on the maximum generated force and torque. *Int J Adv Manuf Technol* 47(1–4):201–215
5. Su H, Wu CS, Pittner A, Rethmeier M (2013) Simultaneous measurement of tool torque, traverse force and axial force in friction stir welding. *J Manuf Process* 15(4):495–500
6. Jonckheere C, de Meester B, Denquin A, Simar A (2013) Torque, temperature and hardening precipitation evolution in dissimilar friction stir welds between 6061-T6 and 2014-T6 aluminum alloys. *J Mater Process Technol* 213(6):826–837
7. Longhurst WR, Strauss AM, Cook GE, Fleming PA (2010) Torque control of friction stir welding for manufacturing and automation. *Int J Adv Manuf Technol* 51(9–12):905–913
8. Cui S, Chen ZW, Robson JD (2010) A model relating tool torque and its associated power and specific energy to rotation and forward speeds during friction stir welding/processing. *Int J Mach Tools Manuf* 50(12):1023–1030
9. Manvatkar VD (2012) Neural network models of peak temperature, torque, traverse force, bending stress and maximum shear stress during friction stir welding. *Sci Technol Weld Join*
10. Yi D, Onuma T, Mironov S, Sato YS, Kokawa H (2016) Evaluation of heat input during friction stir welding of aluminium alloys. *Sci Technol Weld Join* 22(1):41–46
11. Vignesh RV, Padmanaban R, Arivarasu M, Thirumalini S, Gokulachandran J, Ram MSSS (2016) Numerical modelling of thermal phenomenon in friction stir welding of aluminum plates. *IOP Conf Ser Mater Sci Eng* 149:012208
12. Zhu XK, Chao YJ (2004) Numerical simulation of transient temperature and residual stresses in friction stir welding of 304L stainless steel. *J Mater Process Technol* 146(2):263–272
13. El-Sayed MM, Shash AY, Abd Rabou M (2017) Heat transfer simulation and effect of tool pin profile and rotational speed on

- mechanical properties of friction stir welded AA5083-O. *J Weld Join* 35(3):35–43
14. Khandkar MZH, Khan JA, Reynolds AP (2013) Prediction of temperature distribution and thermal history during friction stir welding: input torque based model. *Sci Technol Weld Join* 8(3): 165–174
 15. El-Sayed MM, Shash AY, Abd-Rabou M (2018) Finite element modeling of aluminum alloy AA5083-O friction stir welding process. *J Mater Process Technol* 252:13–24
 16. Meyghani B, Awang M, Emamian S, Khalid NM (2017) Developing a finite element model for thermal analysis of friction stir welding by calculating temperature dependent friction coefficient. 107–126
 17. Su H, Wu CS, Pittner A, Rethmeier M (2014) Thermal energy generation and distribution in friction stir welding of aluminum alloys. *Energy* 77:720–731
 18. Sedmak A, Kumar R, Chattopadhyaya S, Hloch S, Tadic S, Djurdjevic A, Cekovic I, Donceva E (2016) Heat input effect of friction stir welding on aluminium alloy AA 6061-T6 welded joint. *Therm Sci* 20(2):637–641
 19. Lambiase F, Genna S, Leone C, Paoletti A (2017) Laser-assisted direct-joining of carbon fibre reinforced plastic with thermosetting matrix to polycarbonate sheets. *Opt Laser Technol* 94:45–58
 20. Assidi M, Fourment L, Guerdoux S, Nelson T (2010) Friction model for friction stir welding process simulation: calibrations from welding experiments. *Int J Mach Tools Manuf* 50(2):143–155
 21. Ulysse P (2002) Three-dimensional modeling of the friction stir-welding process. *Machin Tools Manuf* 42:1549–1557
 22. Reynolds AP, Tang W, Khandkar Z, Khan JA, Lindner K (2013) Relationships between weld parameters, hardness distribution and temperature history in alloy 7050 friction stir welds. *Sci Technol Weld Join* 10(2):190–199